communications earth & environment

Article

https://doi.org/10.1038/s43247-024-01556-8

Plug flow and brecciation in volcanic conduits can emerge from shear-induced crystal migration in otherwise Newtonian magmas

Check for updates

Jérémie Vasseur[1], Fabian B. Wadsworth[2], Donald B. Dingwell[1] & Yan Lavallée[1]

In the Earth, the flow of crystal-bearing magma is thought to be non-Newtonian and shear thinning, but the physical origin for this is poorly understood. We use hydro-granular theory to show that the decoupled migration of crystals toward conduit cores during magma ascent is a tenable microphysical mechanism for plug flow, emergent in an otherwise purely Newtonian crystal-bearing magma. We use a numerical conduit model to define the flow development length beyond which crystal migration dominates and strain localises near conduit margins. Applied to magma ascent scenarios, we show that this crystal-migration strain localisation only develops in high crystallinity magmas or magmas ascending in very narrow cracks/conduits. In all other scenarios, crystals do not contribute to non-Newtonian behaviour and such magmas are usually strictly Newtonian. The ascent of very crystal-rich dome magma could be associated with strain localisation and crystal depletion at the conduit margins, lubricating ascent through the crust.

Magma rheology is a first-order control on crustal magma ascent dynamics and the style of eruption at the Earth's surface[1]. From a material perspective, magmas are silicate melts in which solid crystals and gas bubbles/pores are suspended, such that continuum models for the multiphase rheology of this mixture are required[2]. While the microphysical effect of suspended bubbles is relatively well understood and based on theory[3,4], crystal-bearing magma rheology remains empirical[5,6]. There are outstanding questions about the role played by non-Newtonian effects[2,7,8] and how these might be upscaled to real magma flow conditions.

Proximal volcanic structures (e.g., lava domes), resulting from crystal-rich magmas, ubiquitously exhibit textural evidence for strain localisation near conduit/flow margins[9–11], argued to result from a rate-dependent or non-Newtonian behaviour of magma shearing under complex, transient conditions[11–13]. Numerical models for crystal-bearing magma ascent and eruption typically assume Newtonian rheology for the effect of crystals on magma viscosity[14–16], such that the crystal-bearing magma rheology depends only on the crystal volume fraction ϕ and several empirical constants[6]. By contrast, existing rheological data show that both non-magmatic suspensions of solid particles[8,17,18] and magmatic suspensions of solid crystals[5–7,19–23] can exhibit apparent non-Newtonian bulk shear-thinning behaviour – a relative drop in suspension viscosity at high shear strain rates relative to low shear strain rates[24]. The origin of this shear thinning is poorly understood and, in some cases, may be a compound effect of an unrelaxed melt response[25,26], viscous heating[27], or cracking of the crystals or magma[28,29]. Therefore, magma ascent models likely use overly simplistic crystal-bearing magma rheology compared with observations of microphysical phenomena. A primary outstanding issue is that of the ultimate microphysical cause of non-Newtonian behaviour in crystal-bearing magmas[30].

Here, we draw on models for non-magmatic particle suspension dynamics and use shear-induced particle migration models built for the generalised flow of particle suspensions in confined geometries such as slots and pipes[31,32]. We aim to explore how the physical movement of crystals relative to the viscous melt – termed shear-induced migration – can result in a more complex bulk response, perhaps more consistent with the complexities observed in rheological tests on magma. Our principal aims are to (1) provide a tenable microphysical origin for plug flow and associated strain localisation arising from crystal effects, and (2) develop the upscaling required to apply this to the conditions of magma ascent.

[1]Earth and Environmental Sciences, Ludwig-Maximilians-Universität, Munich, Germany. [2]Earth Sciences, Durham University, Durham, UK.
e-mail: j.vasseur@lmu.de

Results

A hydro-granular micro-physical model shows that *homogeneous* crystal-bearing magmas are Newtonian

Using a novel experimental apparatus in which the value of particle volume fraction ϕ in a flowing suspension could change as a function of the bulk shear strain rate $\dot{\gamma}$, ref. 17 found that the particle suspensions appear to be Newtonian even at very high ϕ. In their experiments, a permeable plate separates the particle-bearing suspension from a region of clear fluid, so that fluid can pass between the suspension zone and the clear fluid zone. This porous plate is held at a fixed pressure P normal to the plate such that the resulting particle normal stress σ_n – the particle-particle repulsive stress that arises from particle interactions – is directly equal to the constant P. During flow imposed by shear stress τ, the permeable plate moves up and down, transferring fluid into or out of the suspension region. This apparatus showed that when the volume of the shearing system is not fixed and when instead P is fixed, suspensions dilate or contract under shear such that ϕ is a function of τ (or, equivalently, of $\dot{\gamma}$).

The observations made by the authors of ref. 17 led them to infer that if particles are permitted to organise themselves during flow, and the suspension is allowed to dilate or contract locally, then the rheology is universally Newtonian, even at very high ϕ. The implication is that more traditional rheology measurements – in which the suspension's crystallinity is fixed – yield apparent non-Newtonian results only because of local reorganisation within the sample itself that develops into heterogeneity. This further implies that it is possible that shearing samples at high ϕ in fixed-ϕ geometries have been internally heterogeneous at steady state and that the rheological determinations are not indicative of the behaviour at any given local ϕ.Importantly, ref. 17 found that Newtonian behaviour extended to values of ϕ that were within a few per cent of ϕ_j, where ϕ_j is the upper limit of ϕ beyond which the system is jammed and cannot flow as a suspension (sometimes termed a 'maximum packing').

Based on their experiments, ref. 17 identified that the timescale characteristic of particle movement in the fluid is $\lambda_p = \eta_f/\sigma_n$, where η_f is the viscosity of the liquid suspending the particles. The timescale characteristic of the shearing motion is $\lambda_f = 1/\dot{\gamma}$. The ratio of these timescales is termed the 'viscous number' $J = \lambda_p/\lambda_f = \eta_f\dot{\gamma}/\sigma_n$ such that at $J \gg 1$, the hydrodynamic timescale is short relative to the time for viscous particle rearrangement, and so the particles are driven into a homogeneous sheared configuration. By contrast, at $J \ll 1$, the particle rearrangement timescale is short compared with the shearing timescale, and so σ_n acts to dilate or contract the particle pack and particle rearrangements dominate. By developing a system in which P, and so σ_n, could be held constant, the novelty of their experiments was that ref. 17 could experimentally constrain how σ_n depends on the properties of the system and proposed

$$\sigma_n = \eta_f\dot{\gamma}\left(\frac{\phi_j}{\phi} - 1\right)^{-2} \tag{1}$$

where $\phi_j = 0.585$ was observed directly for spheres[17]. This description matches experimental data across the range of ϕ from dilute ($\phi \to 0$) to concentrated ($\phi \to \phi_j$) regimes[17,31,33,34]. Injecting Eq. 1 into the scaling for the viscous number (see above) results in a functional form for J that only depends on ϕ as $J(\phi) = (\phi_j/\phi - 1)^2$ (note that, for $\phi \geq \phi_j$, $J(\phi) = 0$). Therefore, the interpretation of this scaling is that J controls the equilibrium ϕ via dilation or contraction of the pack of particles locally.

Given that this picture of particle suspension rheology depends on the normal stress σ_n and not just the shear stress τ, ref. 17 drew an analogy with granular rheology and introduced a friction coefficient $\mu = \tau/\sigma_n$, which, along with J and ϕ_j, controls the rheology. By using the 'friction' concept, ref. 17 could unify the dilute regime when ϕ is small, where friction comes from internal friction in the fluid suspension, with the concentrated regime at high ϕ, where friction comes dominantly from particle-particle contacts and the lubrication of the fluid is less important. That is, viscous suspensions and dry granular media can be unified by using the friction coefficient.

The friction coefficient μ can be understood as the sum of (1) a contribution arising from particle contacts μ_c similar to that of dry granular media and (2) a hydrodynamic contribution μ_h arising from the dilute regime. Using the dataset of ref. 17, ref. 31 proposed a semi-empirical function that relates μ, ϕ, and J (which is a modification of the original function proposed by ref. 17)

$$\mu = \underbrace{\mu_1 + \frac{\phi_j}{\beta}\left(1 - \frac{\phi}{\phi_j}\right)}_{\mu_c} + \underbrace{\left[J + \left(\frac{5}{2}\phi_j + 2\right)J^{\frac{1}{2}}\right]\left(1 - \frac{\phi}{\phi_j}\right)^2}_{\mu_h} \tag{2}$$

where $\mu_1 = 0.3$ is the value of μ at $\phi = \phi_j$, and $\beta = 0.158$ is the so-called compressibility of the particle pack[31,32]. The value β is justified because $\phi(\mu = 0) = \phi_j + \mu_1\beta = \phi_m$, where ϕ_m is the maximum packing of a pack of compressed particles more organised than a loosely jammed pack at ϕ_j (i.e., $\phi_m > \phi_j$). Using the values given here, $\phi_m = 0.632$ is consistent with the limiting value found for spheres in a flowing but fixed-ϕ setup[18]. With these inputs, Eq. 2 provides an excellent description of these data when converted to the dimensionless space of μ, ϕ, and J (Fig. 1).

Recast as the more familiar 'relative viscosity' $\bar{\eta} \equiv \eta/\eta_f = \mu/J$ this model (Eq. 2) is consistent in terms of functional form with most previous theoretical models[2]

$$\bar{\eta} \equiv \frac{\eta}{\eta_f} = \frac{1}{J}\left[\mu_1 + \frac{\phi_j}{\beta}\left(1 - \frac{\phi}{\phi_j}\right)\right] + \left(1 + \frac{5}{2}\phi + \frac{\phi}{\phi_j}\right)\left(1 - \frac{\phi}{\phi_j}\right) \tag{3}$$

where η is the shear viscosity of the particle suspension. By design, Eq. 3 converges to the Einstein viscosity $\bar{\eta} = 1 + 5\phi/2$ at $O(\phi)$ and diverges with $(\phi_j - \phi)^{-2}$ at $\phi \to \phi_j$, like alternative models such as the ref. 35 scaling $\bar{\eta} = (1 - \phi/\phi_j)^{-2}$.

In Fig. 1, we follow refs. 17, 31 and show the results of applying the hydro-granular theory to experimental results for the rheology of suspensions of spherical particles in viscous liquids. We find that Eq. 2 accurately describes how the relevant stresses μ are related to the particle volume fraction ϕ (via the compressibility β, the viscous number $J(\phi)$, and the limit jamming fraction ϕ_j). While our analysis of $\mu(J, \phi)$ should be limited to the few cases of experimental datasets where σ_n is known[17,33], by converting $\mu(J, \phi)$ to $\bar{\eta}(\phi)$ (see Eq. 3), we can plot additional published data and test Eq. 3 across a broader range of ϕ (Fig. 1d). We find generally good agreement, albeit with some data scatter at $\phi \approx \phi_j$, which is likely due to the heterogeneity effects that may be prevalent in fixed-ϕ rheometry at high ϕ (discussed above).

The analysis provided in Fig. 1 constrains the driving force for the dilation or contraction of a particle suspension under shear. By design, the experiments underpinning this formulation[17] were at constant σ_n. In contrast, in magmatic scenarios, the initial ϕ at the base of a conduit is more typically considered constant, and σ_n can vary spatially and with time. In such a fixed initial ϕ scenario, σ_n will drive particle movement relative to the liquid so that spatial gradients of σ_n are minimised[31,32] by inducing spatial gradients in ϕ. This framework in which particle-particle pressures arise in fixed-ϕ systems, predicts that under shear in a confined geometry such as a pipe or a slot, particles will migrate from regions of high relative shear strain rates at the walls, toward regions of low or zero relative shear strain rates at the centreline, inducing gradients of ϕ, and therefore gradients of viscosity η. The consequence of such a theory in which particles organise in response to flow, is that plug flow and strain localisation can be an emergent property of an otherwise Newtonian rheology.

Upscaling to conduit flow conditions: a continuum model for crystal migration under an evolving crystal-crystal pressure

The local – or *homogenous* – behaviour of packs of particles can be predicted in full using the hydro-granular framework provided (Fig. 1). This rheology predicts that the volume fraction of the solid phase – crystals in the case of

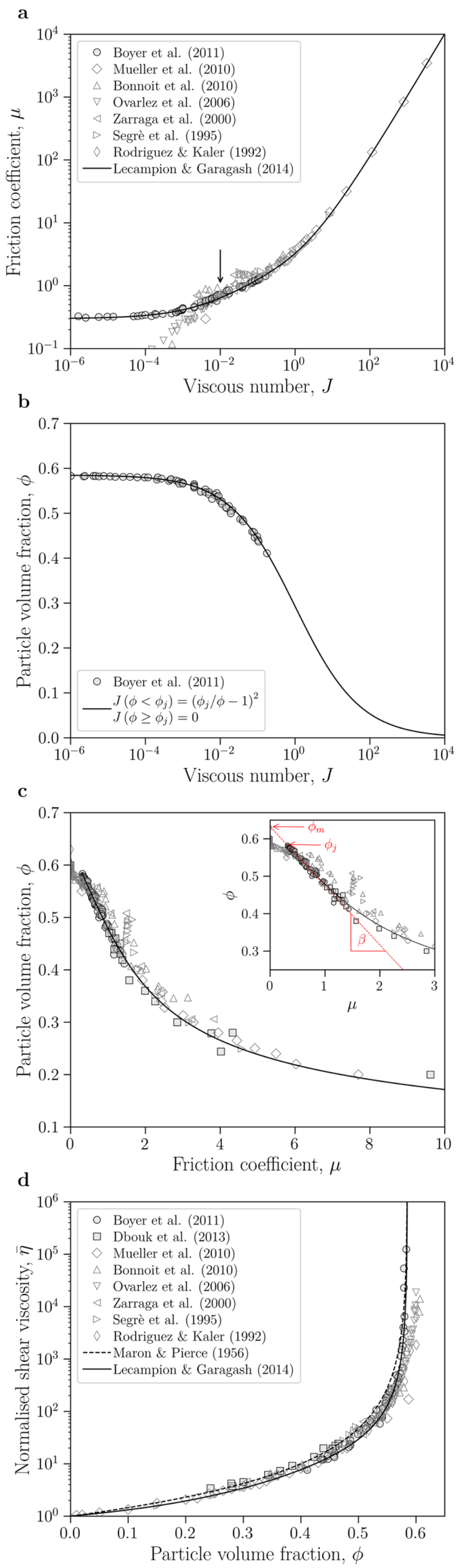

Fig. 1 | Validating the microphysical constitutive description for hydro-granular rheology used here. a The ratio of stresses $\mu = \tau/\sigma_n$ as a function of the viscous number $J = \eta_f \dot{\gamma}/\sigma_n$ (Eq. 2). The arrow indicates where a deviation of the data from the theory can be observed and only occurs for systems where the particle suspension is assumed to be at fixed ϕ, such that the deviation can be interpreted to be associated with the formation of textural heterogeneity during shear. This implies that $J > 0.01$ is the critical viscous number for homogeneous rheometry experimentation at the traditional fixed ϕ. **b** The particle volume fraction ϕ as a function of J. **c** The particle volume fraction ϕ as a function of μ, showing the role played by β in the formulation (see *inset*)[31]. **d** The equivalent formulation as shown in (**a**–**c**), but cast as the more familiar normalised viscosity $\bar{\eta} = \eta/\eta_f$ as a function of ϕ (Eq. 3). In (**a**–**c**) we show the constitutive model $\mu(J)$, $J(\phi)$, and $\mu(\phi)$ given by Eq. 2 and in the text[17,31]. We also plot two types of data: (1) as solid symbols, we plot data for packs of spheres performed in apparatuses in which P is either constant or measured[17,33], and (2) as unfilled pale symbols, we additionally show a range of data for particle suspension rheology[18,65–69] for which ϕ was imposed and not P (i.e., traditional rheometry). In (**d**) we also show the ref. 35 model advocated for magmatic suspensions[2].

magma flow – can locally dilate (i.e., a decrease in local ϕ) or compact (i.e., an increase in local ϕ) in response to changes in the crystal-crystal interaction stress σ_n (Eqs. 1–2). Therefore, this differs from typical approaches to crystal-bearing magma rheology in which the volume fraction ϕ is considered homogeneous and fixed for a given packet of magma. The result of the different approach used here (Fig. 1) is that any conduit flow model must then be set up such that the relative motion of crystals and melt can be tracked in response to local variations in σ_n both laterally across the conduit and vertically down-flow. To do this, we implement a numerical confined flow model[31]. This model assumes that both the liquid and solid components are incompressible and neutrally buoyant, and then takes the continuity equations for the solid phase and the mixture such that a relative slip velocity can be defined. Together with momentum and drag force balance equations, this permits a full solution to be found. The full model is described in the "Methods" section and elsewhere[31]. Here, we note the characteristic scales that dictate the regimes of behaviour

$$\begin{aligned}&\bar{t} = \frac{tU_0}{H}; \bar{y} = \frac{y}{L}; \bar{z} = \frac{z}{H}; \bar{v}_y = \frac{v_y}{\delta U_0}; \bar{v}_z = \frac{v_z}{U_0};\\ &\bar{\dot{\gamma}} = \frac{\dot{\gamma}L}{U_0}; \bar{\tau} = \frac{\tau L}{\eta_f U_0}; \bar{p} = \frac{p\delta L}{\eta_f U_0}; \bar{p}_s = \frac{p_s L}{\eta_f U_0}; \bar{p}_f = \frac{p_f \delta L}{\eta_f U_0}; \bar{q} = \frac{qL^2}{U_0 a^2}\end{aligned} \tag{4}$$

where a bar above a parameter denotes a dimensionless – or scaled – variable, and the subscripts 's' and 'f' refer to solid and fluid, respectively. t is the time, U_0 is the inlet velocity, H is a vertical length scale taken here to be $H = L^3/a^2$, y is the horizontal position ($y \equiv x$ for a 'slot' geometry and $y \equiv r$ for a 'pipe' geometry), L is the conduit width (either the dyke half-width in the case of a 'slot' geometry $L \equiv W$ or the cylindrical conduit radius in the case of a 'pipe' geometry $L \equiv R$), z the vertical position, v_y and v_z are the mixture velocities in the two directions, $\dot{\gamma}$ and τ are the local shear strain rate and stress, respectively, p is the pressure, q is the relative phase flux, and a is the crystal size (taken as a characteristic radius). Here, $\delta = L/H = (a/L)^2$ is a characteristic aspect ratio of the flow. We note that in real magmatic scenarios, the crystals are not necessarily neutrally buoyant and that density differences may be important, especially when considering the relative phase flux, as done here. Future work should consider density contrast and buoyancy effects.

We solve the system of equations to predict both flow in a dyke (i.e., 'slot' geometry) and a cylindrical conduit (i.e., 'pipe' geometry) to illustrate the principal features of the shear-induced particle migration process (Fig. 2). These solutions are cast in dimensionless form, such that the lengths and pressures involved are all scaled by characteristic parameters (Eq. 4). The model shows that the inlet crystal volume fraction $\phi_0 = \phi(z = 0)$ at the base of the slot or pipe is uniform but develops down-flow via shear-induced migration. Both the degree to which this particle organisation occurs and the distance down-flow that is required to reach *fully developed* flow depend on ϕ_0 and the geometry (dyke or cylindrical conduit) on no other variables once the normalisations in Eq. 4 are established. Therefore, the results in Fig. 2 are universal for a given ϕ_0 inlet value. Ref. 31 showed that this solution is well-validated against direct measurements of particle organisation at steady state in flow along a pipe[36]. Both those experimental results and the continuum fluid dynamic solution show that (1) particles move during flow from the wall regions to the centre-line region, (2) the velocity profile blunts to produce plug flow even with locally Newtonian rheology, and (3) the plug density (i.e., the ϕ in the plug) increases above ϕ_j toward a random close

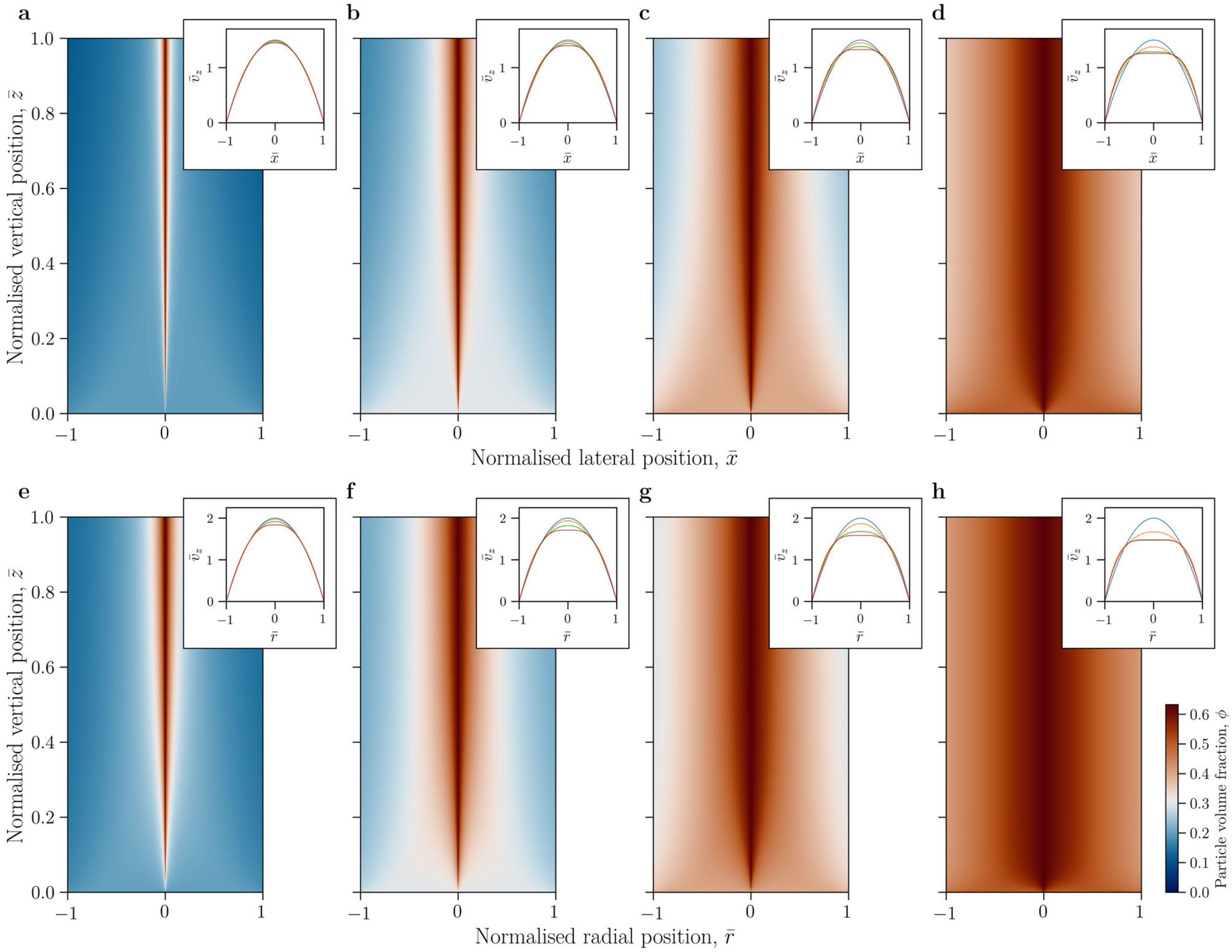

Fig. 2 | Normalised conduit model outputs for shear-induced crystal migration and the development of plug flow. a–d The result for flow in a dyke geometry. **e–h** The result for flow in a cylindrical conduit. The inlet crystal volume fraction is homogeneous at $\bar{z} = 0$ and is set to $\phi_0 = 0.2$ in (**a**, **e**) $\phi_0 = 0.3$ in (**b**, **f**) $\phi_0 = 0.4$ in (**c**, **g**) and $\phi_0 = 0.5$ in (**d**, **h**). *Insets*: The radial distribution of vertical mixture velocities at four different snapshots of vertical position at $\bar{z} = 0$ (blue line), $\bar{z} = 0.01$ (orange line), $\bar{z} = 0.1$ (green line), and $\bar{z} = 1$ (red line), illustrating the blunted velocity profile characteristic of plug flow development and lubricated conduit margins.

pack $\phi_m \approx 0.632$ – the higher density predicted for more ordered packs[18,37]. This demonstrates that a continuum model that upscales the local *homogeneous* rheology as the origin of the pressures driving particle motion, can predict bulk larger-scale *heterogeneous* effects including flow-driven organisation of particles.

The model used here has been validated against previous pipe- and slot-flow data[36,38,39] including in high-resolution magnetic resonance imaging experiments of pipe flow[32]. These detailed validation steps provide confidence that the conduit model described here can be used to make predictions about real-world particle migration scenarios where particle migration is driven by shear-induced processes. In all cases tested the data and the predictions match well. When combined with the existing microstructural validation of these ideas (see Fig. 1), we propose that this model is sufficiently robust to upscale to magmatic conduits.

Discussion

Application to magmatic systems

The analysis in the previous section demonstrates that it takes a finite distance of flow for particle suspensions to organise themselves (Fig. 2). If the flow distance in a real scenario is less than the distance required for organisation to occur, then the suspension will effectively remain close to the uniform initial particle volume fraction, and the bulk average flow will be Newtonian. However, if there is sufficient distance available for the suspension to organise itself via particle migration, then the bulk behaviour across the slot or pipe will be apparently non-Newtonian, even though the local rheology imposed here is strictly Newtonian. Therefore, a key question in the application to magmatic conditions is: under what conditions do magmatic flows travel a sufficient distance to organise? This question is key to upscaling from the concept of particle – or crystal – migration to the effective rheology of magmas in the crust.

To answer the question posed here, we can assess the axial flow development length that is characteristic of the transition from a Poiseuille-type velocity profile relatively near the inlet to a blunted velocity profile once flow has developed to full organisation (see the insets to Fig. 2). The critical scaling is the length scale from the slot or pipe base to the point at which the flow is fully developed – a length termed the development length L_d. This can be captured by the scaling[31]

$$L_d \propto \frac{L^3}{a^2}\frac{J(\phi_0)S(\phi_0)}{\kappa(\phi_0)} \tag{5}$$

where $S(\phi)$ is a so-called inelastic storage coefficient that arises from the rheology, and $\kappa(\phi)$ is a dimensionless scaling for the effective permeability of melt between the crystals that influences the crystal mobility. Here, $\kappa(\phi) = 2(1-\phi)^{\alpha}/(9\phi)$ with $\alpha = 5.1$ as an experimentally validated value[31,40]. The parameter $S(\phi)$ relates to μ and is $S(\phi) = -(\mu/\phi)\mathrm{d}\phi/\mathrm{d}\mu$

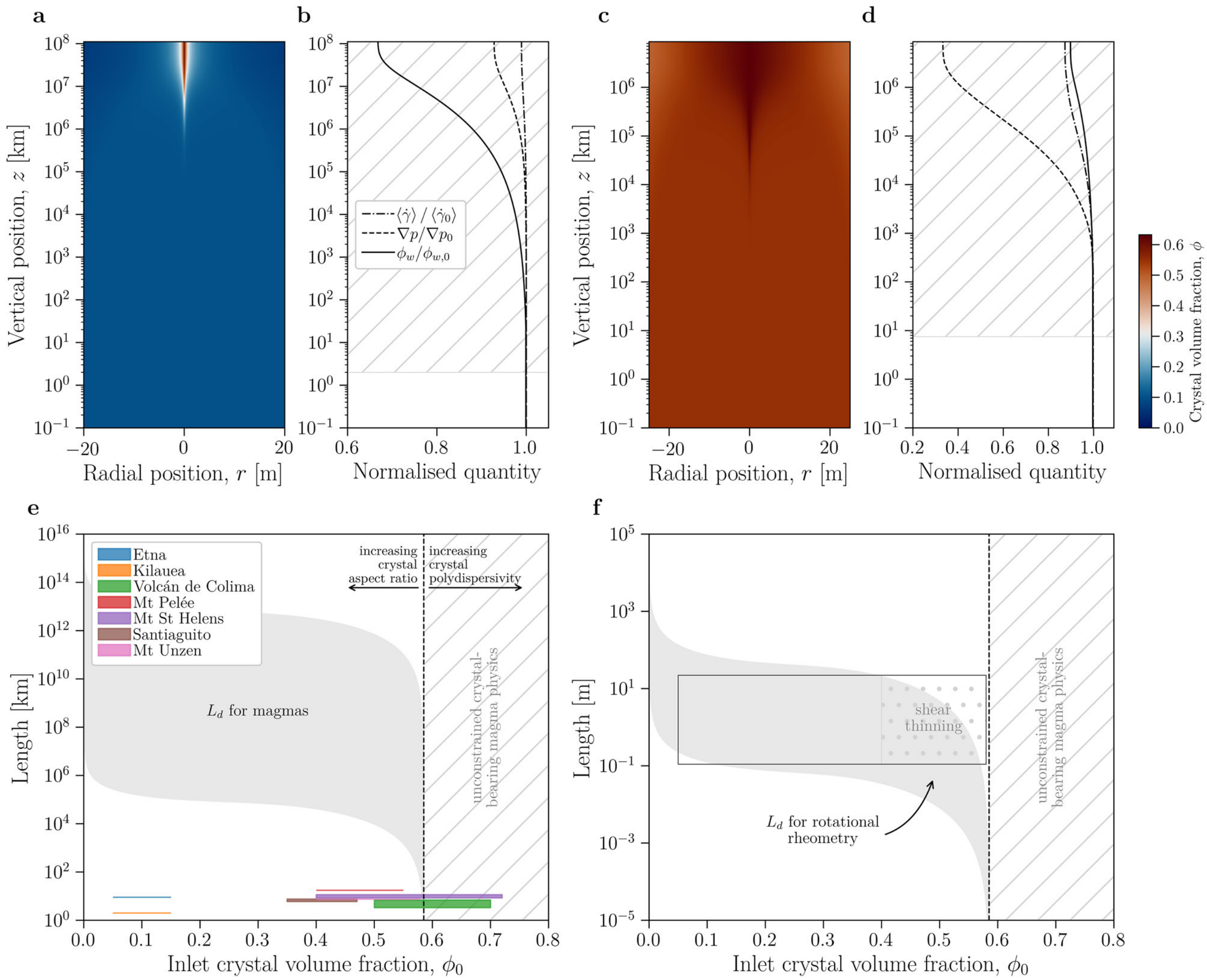

Fig. 3 | Applications of the conduit flow model (Fig. 2) to volcanic and experimental scenarios. a, b The result of an application to a typical basaltic conduit using inputs for Kilauea volcano (USA) of $\phi_0 = 0.1$, $a = 600$ μm, $R = 20$ m, and $L_f = 2$ km, where **a** shows the dimensional up-conduit development of ϕ (as per Fig. 2) and **b** shows the up-conduit development of the values of the crystal volume fraction at the wall ϕ_w, the mixture pressure gradient ∇p, and the gap-averaged strain rate $\langle \dot{\gamma} \rangle$, all normalised to the inlet values of those metrics. **c, d** The same as in (**a, b**) but for a typical case of a silicic conduit, here using input values for Mt Unzen (Japan) of $\phi_0 = 0.55$, $a = 300$ μm, $R = 25$ m, and $L_f = 7.5$ km. In (**b, d**), we use hatching to show the region of the system greater than L_f, which is, therefore, inaccessible; this implies that shear-induced migration is unlikely in both scenarios. **e** A compilation of these findings for a range of volcanic conduits in the upper crust where we compare L_f from literature values for total estimated conduit lengths[1] with the model predictions for the length required for shear-induced crystal migration L_d. Overall, these results highlight that crystal-rich magmas can have L_f values that intersect with a range of possible L_d results. We note that there is substantial uncertainty in ϕ_j for natural magmas. **f** The same result as in (**e**) but for experimental rheometry, demonstrating that in many cases (e.g., ref. 18) the shearing distance (computed from minimum strains) is sufficient to induce migration during their experiment, explaining why they appear to find shear thinning in what should otherwise be a Newtonian condition (cf. ref. 17).

(described in the "Methods" section). Importantly, J, S, and κ are only functions of the particle volume fraction ϕ.

The development length L_d can be predicted by Eq. 5 and is a measure of the vertical flow distance required for crystal migration to play a substantial role in modifying the flow rates of crystal-bearing magma. By compiling L and ϕ_0 for realistic magmatic conduit flow scenarios and by taking a wide range $10^{-5} \le a \le 10^{-3}$ m for suspended crystal sizes in magmas, we can use Eq. 5 to estimate L_d. For those same systems, we use petrologic estimates of storage depths measured from the Earth's surface[1] as a first-order conservative constraint on the natural flow distance available between shallow storage and an eruption, termed L_f. The key test we apply here is whether or not L_d is shorter than the length available L_f.

We find that where ϕ is very close to ϕ_j, $L_d \lesssim L_f$; a regime in which crystal migration will occur, plug flow will develop, and strain localisation will be the outcome at the conduit walls (Fig. 3). This $\phi \approx \phi_j$ state is typical of dome-forming lavas[41]. The shear-induced migration regime of magma ascent is also accessible for very narrow conduits; for example, if a conduit is less than 1 m in diameter, shear-induced crystal migration is likely even at moderate to low ϕ. Outside of the high-ϕ concentrated and semi-mushy magmas, at most ϕ and L applicable in the crust, $L_d \gg L_f$ (Fig. 3) and L_d is around 4–12 orders of magnitude in excess of the conduit lengths. In turn, this implies crystal migration is not likely to occur for these low or moderate crystallinities because there simply is not the flow distance available to fully develop plug flow. Therefore, for these cases, a Newtonian contribution of crystals to the bulk magma rheological in the crust is sufficient.

We can also compute L_d for some experimental approaches, which allows us to rationalise why apparent shear thinning is reported in such work[18]. To do so, we take L in Eq. 5 as the gap width in the rheometer used, and a to be the experimental particle size. To take one example, ref. 18 reports strains in excess of 200 in a parallel plate set up with a 1.5-mm gap width and 35-mm diameter. This implies that the minimum rotational distance is ~22 m, which is within the range where migration can occur

(Fig. 3). For this reason, we anticipate that shear-induced migration of particles and the associated development of heterogeneity in samples during flow is a tenable explanation for the shear thinning observed by ref. 18. If correct, these experiments align with the other approaches discussed herein[17].

Our result implicates high crystallinity dome magmas as a magmatic scenario in which shear-induced crystal migration can occur over possible ascent distances (Fig. 3). For very crystal-rich domes, the prediction of shear-induced migration would be that the dome margins would be relatively depleted in crystals relative to the flow core and the extent of depletion would depend on the ratio L_f/L_d and the conduit inlet crystallinity ϕ_0. Features observed in dome deposits from the 1991–1995 Mt Unzen eruption or the 2004–2008 Mt St Helens eruption show relatively high strain conduit margin facies that could be consistent with this prediction[9,10]. The second regime in which crystal migration can occur over the flow lengths available is magma flow in narrow conduits or dykes. Outside of the conditions explored here (high crystallinity or narrow conduits and dykes), the crystal contribution to magma flow is predicted to be a Newtonian one. This suggests that in situations for which crystal migration is not operative, Newtonian constitutive models for shear viscosity in crystal-bearing magmas[6] are sufficient to capture the crystal effect. Finding real magmatic examples where evidence for crystal migration is preserved is likely to be hampered by cooling-induced lateral crystallinity variations. However, if a given magmatic scenario is likely to be subject to migration (i.e., narrow dykes or high crystallinity magmas), then it will be important to deconvolve migration-induced crystallinity variations from cooling-induced crystallinity variations.

Gravitational spreading of crystal-rich conduit cores

We find that crystals can migrate toward conduit cores, especially for conduits that have a high initial crystallinity and/or for narrow dykes/conduits (Fig. 3). However, because magmatic crystals are typically denser than the melt phase (by a density ratio of up to $\Delta\rho \approx 600$ kg.m^{-3}; see ref. 42), gravity can act to spread the dense crystals out and minimise the lateral variations in ϕ that we predict. To check this, we compare the lateral variations in hydrostatic pressure with the lateral gradient of the normal stress σ_n. By tracking these two gradients in pressure – one driving crystal migration and the other opposing migration – we can assess the conditions under which crystal migration will be operative in magmatic cases. Taking Mt Unzen as a test case, we find that if the melt viscosity and inlet velocities are at the high end of the range permitted by published predictions (i.e., $U_0 \geq 0.01$ m.s^{-1} and $\eta_f \geq 10^7$ Pa.s; see ref. 1) and if the conduit is moderately narrow (i.e., $R \approx 10$ m; see refs. 43,44) then migration can occur without significant gravitational spreading (see "Methods" section). If instead, the melt viscosity and the inlet velocity are lower, then gravitational spreading becomes important and can counteract the migration physics invoked herein. This is consistent with our finding that for volcanoes such as Kilauea, migration is negligible anyway because the real-world conduit/dyke is simply too short for development of migration to onset (Fig. 3). If the conduit *were* long enough, then at the low melt viscosities required for Kilauea and the higher relative $\Delta\rho$ of mafic systems, gravitational spreading would certainly be important, and migration could not occur. By definition, the lateral gradient in the normal stress σ_n driving migration always becomes small as flow fully develops, such that gravitational spreading will always 'take over' as flow fully develops. However, one of our key findings is that in nature, the conditions for fully developed flow are rarely, if ever, reached because the real-world conduits are not sufficiently long.

The findings explored here allow us to reiterate that migration is particularly important for systems at which (i) the conduit is nominally narrow, (ii) the melt viscosity, the crystallinity, and the inlet velocities are relatively high; and (iii) there is sufficient vertical length from storage to the surface so that development of migration profiles can occur. For systems that do not fit these three requirements, the flow is Newtonian and not influenced by migration.

Brittle localised brecciation of crystal-bearing magma at conduit walls

Here, we use this conduit model to predict the brittle onset of shear brecciation in cylindrical conduit-filling magma. The brittle onset is found by tracking the bulk (i.e., crystal-bearing mixture) strain rate $\dot{\gamma} = \mathrm{d}v_z/\mathrm{d}r$ at all locations in the conduit flow simulations and comparing this with the viscoelastic threshold for localised failure $\dot{\gamma}_c = \mathrm{Wi}_c G/[\eta_f \mathscr{L}(\phi)]$, where Wi_c is the critical constant for melt failure (taken from the linear viscoelastic theory associated with the Weissenberg number Wi, and with a value constrained to be $\mathrm{Wi}_c = 0.01$; see refs. 20, 25, 26, 45), $G \approx 10$ GPa is the shear modulus of magmatic liquids[46], and $\mathscr{L}(\phi)$ is the so-called lever function[25] that accounts for the amplification of the melt strain rate around crystals. Ref. 25 gives two options for the definition of $\mathscr{L}(\phi)$, both consistent with available data, and so here we take the minimal model $\mathscr{L}(\phi) = \bar{\eta}(\phi)$ (see Eq. 3). If the local mixture strain rate $\dot{\gamma}$ exceeds this constraint of the critical strain rate $\dot{\gamma}_c$, then the melt between the crystals is predicted to break, and the magma can be considered brecciated.

Given that the velocity gradients in the radial direction are always steepest at the conduit walls, shear failure occurs first at that location. Whether or not rupture occurs depends on the inlet velocity U_0 such that at low relative U_0 values, no shear failure occurs, and flow is purely viscous at all conduit locations. Conversely, at high relative U_0 values, shear failure occurs at the conduit walls. These two possibilities are separated by a critical value of U_0 above which rupture occurs. In Fig. 4, we plot the ratio between these critical values and the conduit radius R, giving a conduit strain rate U_0/R. We find that for a given inlet crystallinity ϕ_0, the critical condition for shear failure is an inverse function of the melt viscosity η_f with a proportionality $U_0/R \propto \eta_f^{-1}$. We use this observation of how these parameters are related to fit an emulator function to the simulation results of the form $U_0/R = C G \eta_f^{\beta}$. Here, C and β are fit parameters for a range of ϕ_0 values. We then find that, remarkably, β is always a constant corresponding to $\beta = -1$ and that C is a continuous, monotonic function of ϕ_0 for which we, in turn, propose the scaling $C(\phi_0) = C_0(1 - \phi_0/\phi_j)^{\alpha}$ with best-fit $C_0 = 2.6 \times 10^{-3}$ and $\alpha = 1.75$ (see *inset* to Fig. 4). [We note that ref. 16 found that $\beta = -0.9$, which leads to issues around the units of C (i.e., that they are (Pa.s)$^{-0.1}$), whereas our $\beta = -1$ implies that C is dimensionless.]

We propose that our failure solution for U_0/R is useful for predicting the conditions under which conduit brecciation will occur at the conduit inlet. In Fig. 4, we show some natural magma conditions of η_f and U_0/R. To find these, we refer to ref. 1, who find that across most silicic compositions (andesite, dacite, and rhyolite), the ascent velocity range for effusive eruptions spans approximately $10^{-5} \leq U_0 \leq 10^{-1}$ m.s^{-1}, which defines our conditions of interest. We use $5 \leq R \leq 50$ m and a range $10^6 \leq \eta_f \leq 10^8$ Pa.s for wet rhyolite ascending the crust[47]. In this case, our model predicts that shear brecciation is likely if ϕ_0 is high. For comparison, we additionally plot the same case but for $10^9 \leq \eta_f \leq 10^{11}$ Pa.s, which corresponds to a similar ascent scenario but one in which the melt has degassed, perhaps due to bubble nucleation and growth (although note that we are not simulating the effect of bubbles explicitly). In this case, a much wider range of ϕ_0 values is in the regime where ascent-driven brecciation will occur (note that if $\eta_f \gtrsim 10^{10}$ Pa.s, brecciation is inevitable for almost all crystallinities). The boxes for natural conditions given in Fig. 4 are informed by natural case studies but designed to be general guides to silicic magma ascent. Note that we simply find the critical strain rate for brecciation at the wall, and do not explicitly model the dynamics of flow of brecciated magma (i.e., we take the same one-way coupling approach as ref. 16).

Conclusions

The model we present here is a 'toy model' for exploring a process and assessing its impact on conduit flow feeding volcanic eruptions. That is, we do not aim to simulate natural processes in full. Instead, we aim to make a quantitative assessment of whether crystal migration is likely to affect conduit flow, or not. The conclusion of this assessment is that magma flow in narrow or very long conduits in the crust may be subject to crystal migration and that this effect will be most prevalent for relatively high

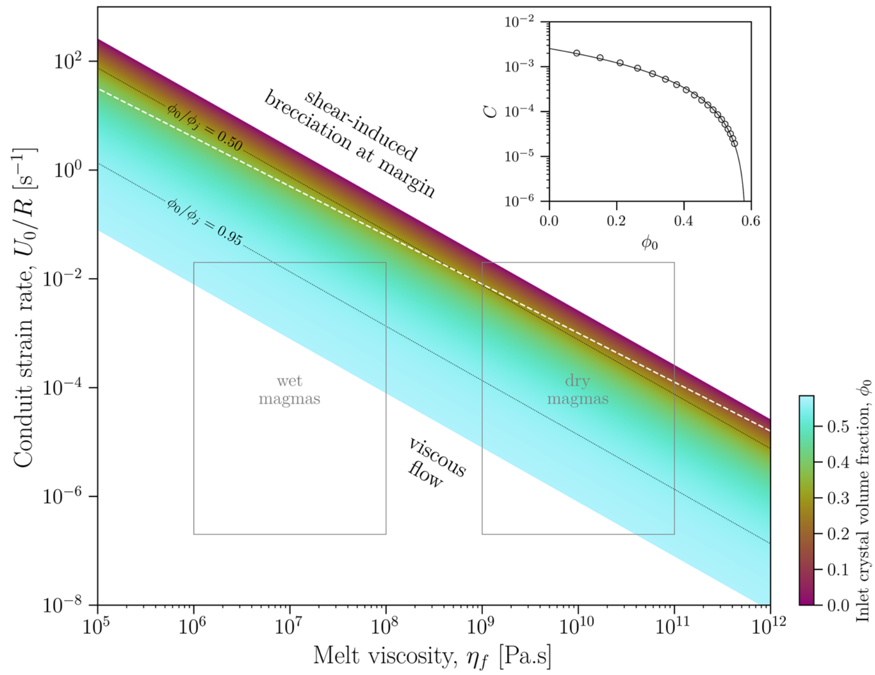

Fig. 4 | The predicted conditions required for brecciation at conduit walls during silicic magma ascent. For a given ϕ_0 and η_f there is a single critical U_0/R value above which the strain rate $\mathrm{d}v_z/\mathrm{d}r$ at $r = \pm R$ exceeds the criterion $\mathrm{Wi}_c G/[\eta_f \mathscr{L}(\phi)]$; here, these critical values of U_0/R are plotted as a continuous function of η_f and colour-coded for ϕ_0. We pick out two values of ϕ_0/ϕ_j to plot as thin dotted black lines ($\phi_0/\phi_j = 0.50$ and $\phi_0/\phi_j = 0.95$). We plot two boxes designed to represent 'wet' magmas[1,47] and nominally 'dry' magmas[1,45], respectively, for silicic effusive eruptions (see text). We also plot the ref. 16 solution $U_0/R = 10^{-4} G\eta_f^{-0.9}$ as the white dashed line (note that in print, ref. 16 quote their law as $U_0/R = 10^{-2} G\eta_f^{-0.9}$, whereas we find that to reproduce their curve, we require the prefactor to be 10^{-4} and not 10^{-2}). The full solutions are well-matched by an emulator function $U_0/R = C(\phi_0)G/\eta_f$ with $C(\phi_0) = C_0(1 - \phi_0/\phi_j)^\alpha$, for which the best-fits are $C_0 = 2.6 \times 10^{-3}$ and $\alpha = 1.75$. In the *inset*, we plot $C(\phi_0)$ as points for our full solution and as a continuous curve for our emulator function.

crystallinity magmas for which the crystal-crystal pressures are high. Where this could happen, we conclude that it will influence strain localisation and brittle brecciation onsets at conduit margins (Fig. 4). In scenarios where this is unlikely to happen, we conclude that the crystal contribution to magma rheology will likely be Newtonian (see ref. 25). An important limitation in the construction of our 'toy model' for crystal motion in conduits is that we do not consider the effect of density differences between the melt and the crystals, which could play an important additional role in determining their relative velocity. While the vertical pressure gradient dominates over the density-derived horizontal gradients, for horizontal motion of crystals, such density contrasts could be important and warrant study in the future.

While the crystal contribution to magma rheology may be Newtonian in many cases, we acknowledge that other effects can render the magma as a whole non-Newtonian (e.g., due to bubble deformation at intermediate conduit capillary number[3]). Our analysis potentially explains why some experiments have seen non-Newtonian effects (particularly at high crystallinity[5,7,18,28]) and that this is potentially associated with migration-induced and evolving sample crystallinity heterogeneity.

The migration physics implemented, upscaled, and explored here may explain how crystal heterogeneity and banding occur in frozen dyke outcrops[48] and the physics of lithic or xenolith movements[49]. When considering banding picked out by crystallinity changes that cannot be accounted for by cooling-induced crystallisation, more complex crystal migration scenarios than envisaged here may be responsible. For example, if migration occurs during continued flow with a pulsatory inlet velocity such that $U_0 = f(t)$ where t is time. Similarly, xenolith and lithic motion will be subject to the same pressure σ_n as described here for crystals, albeit for a typically larger radius a. These more complex scenarios should be assessed and explored using our model. Additionally, our model provides a mechanism for how phenocrysts may 'swim together' and meet in flow. This process is usually called 'synneusis' but is rarely explained on physical grounds. For example, shear-induced crystal migration could explain how 0.6 mm olivine crystals come to meet and form >1 mm olivine crystal aggregates in the Kilauea system[50].

An important feature of crystal-bearing magmas is that the crystal populations typically have bimodal size distributions with relatively large phenocrysts and relatively small microlites or nanolites. Given that crystal size is a key input to the development length explored here $L_d \propto a^{-2}$, we acknowledge that phenocrysts and microlites will behave differently when it comes to flow development and migration. While our scaling outputs for L_d include a range of crystal sizes from microlites to phenocrysts, we do not account for the interactions between crystals or large and small relative sizes. Such complex interactions could affect the phenomenology of the migration behaviour[51] and are not accounted for here. This problem would be best addressed by using experimentation to examine the phenomenon of migration for bimodal particle sizes.

In natural magma flow, bubble deformation[3,4,52], compressibility effects, syn-transport crystal growth, crystal-melt density differences, crystal plastic deformation[53], viscous dissipation as heat[54], melt shear thinning due to unrelaxed melt structure effects[25], and brittleness[29] all remain candidates for conduit flow effects that would manifest as additional contributions to plug flow development. Importantly, most of these effects are underpinned by theoretical models and so can be upscaled along with the crystal migration effects described here, culminating in both a full theoretical picture of magma flow dynamics in conduits, but also in a regime- or phase-picture of the conduit conditions that would permit the regime of ascent dynamics to be identified for individual conduit scenarios. The crystal migration effect – analysed in isolation here – needs to be embedded in future conduit flow models if ascent rates and conduit dynamics are to be fully predictable. A challenge will be to explore how other phases, such as bubbles or cracks, influence crystal migration.

Methods

Conduit model

Here, we provide a workflow for the conduit model presented in the main text and adapted from ref. 31 (developed for shear-induced particle migration in slot and pipe flow), the initial and boundary conditions for the solution, and our solution method. Defining $\boldsymbol{v}_s$ and $\boldsymbol{v}_f$ as the local average solid and fluid Eulerian velocities, respectively, $\boldsymbol{u} = \phi\boldsymbol{v}_s + (1-\phi)\boldsymbol{v}_f$ as the mixture velocity, and assuming incompressibility of both fluid and solid phases and steady flow, the continuity equations for the conservation of mass and momentum are

$$\begin{gathered}\frac{1}{\phi}\boldsymbol{v}_s\cdot\nabla\phi + \nabla\cdot\boldsymbol{v}_s = 0\\ \nabla\cdot\boldsymbol{u} = \nabla\cdot(\boldsymbol{q}+\boldsymbol{v}_s) = 0\\ \nabla\cdot\boldsymbol{\sigma} + \rho\boldsymbol{g} = \nabla\cdot(\boldsymbol{\tau} - p\boldsymbol{I}) + \rho\boldsymbol{g} = 0\end{gathered} \tag{6}$$

where $\boldsymbol{q} = \boldsymbol{u} - \boldsymbol{v}_s = (1-\phi)(\boldsymbol{v}_f - \boldsymbol{v}_s)$ is the relative phase slip velocity, $\boldsymbol{\sigma}$ is the mixture stress tensor (sum of the fluid and particle stress tensors), ρ is the mixture density, $\boldsymbol{g}$ is the acceleration due to gravity, $\boldsymbol{\tau}$ is the mixture deviatoric stress, p is the mixture pressure and $\boldsymbol{I}$ is the identity matrix. For negligible Reynolds number $\boldsymbol{q} = (a^2\kappa(\phi)/\eta_f)(\nabla\cdot\boldsymbol{\sigma_f} - \rho_f\boldsymbol{g}) = -(a^2\kappa(\phi)/\eta_f)(\nabla p_f\boldsymbol{I} + \rho_f\boldsymbol{g})$, for which $\boldsymbol{\sigma_f}$ is the fluid stress tensor, p_f is the fluid pressure, and ρ_f is the fluid density. In the main text, we neglect the gravity terms (see below 'Effects of body forces arising from gravity') and so Figs. 2–4 do not include this effect. Projecting Eq. 6 onto Cartesian (i.e., slot flow) coordinate system and using the characteristic scales introduced in Eq. 4 results in

$$\begin{gathered}\frac{1}{\phi}\left(\bar{v}_x\frac{\partial\phi}{\partial\bar{x}} + \bar{v}_z\frac{\partial\phi}{\partial\bar{z}}\right) - \frac{\partial\bar{q}_x}{\partial\bar{x}} - \delta\frac{\partial\bar{q}_z}{\partial\bar{z}} = 0\\ \frac{\partial\bar{v}_x}{\partial\bar{x}} + \frac{\partial\bar{v}_z}{\partial\bar{z}} + \frac{\partial\bar{q}_x}{\partial\bar{x}} + \delta\frac{\partial\bar{q}_z}{\partial\bar{z}} = 0\\ \frac{\partial\bar{\tau}_{xx}}{\partial\bar{x}} + \delta\frac{\partial\bar{\tau}_{xz}}{\partial\bar{z}} - \frac{1}{\delta}\frac{\partial\bar{p}}{\partial\bar{x}} = 0\\ \frac{\partial\bar{\tau}_{zx}}{\partial\bar{x}} + \delta\frac{\partial\bar{\tau}_{zz}}{\partial\bar{z}} - \frac{\partial\bar{p}}{\partial\bar{z}} = 0\end{gathered} \tag{7}$$

and, similarly, the relative phase slip vector can be decomposed in

$$\begin{aligned}\bar{q}_x &= -\frac{\kappa}{\delta}\frac{\partial\bar{p}_f}{\partial\bar{x}} = -\kappa\left(\frac{1}{\delta}\frac{\partial\bar{p}}{\partial\bar{x}} - \frac{\partial\bar{p}_s}{\partial\bar{x}}\right)\\ \bar{q}_z &= -\kappa\frac{\partial\bar{p}_f}{\partial\bar{z}} = -\kappa\left(\frac{\partial\bar{p}}{\partial\bar{z}} - \delta\frac{\partial\bar{p}_s}{\partial\bar{z}}\right)\end{aligned} \tag{8}$$

Assuming that a is much smaller than the half-width W of the conduit (i.e., $\delta \ll 1$), Eq. 8 reduces to

$$\begin{aligned}\bar{q}_x &= -\kappa\left(\frac{\partial\bar{\tau}_{xx}}{\partial\bar{x}} - \frac{\partial\bar{p}_s}{\partial\bar{x}}\right) = -\kappa\frac{\partial\bar{\sigma}_n}{\partial\bar{x}}\\ \bar{q}_z &= -\kappa\frac{\partial\bar{p}}{\partial\bar{z}}\end{aligned} \tag{9}$$

Similarly, Eq. 7 reduces to

$$\frac{\partial\bar{\tau}_{zx}}{\partial\bar{x}} = \frac{\partial\bar{p}}{\partial\bar{z}} \tag{10}$$

for the conservation of momentum, implying that $\bar{\tau} = |\nabla\bar{p}|\bar{x}$ (defined as $\bar{\tau} \equiv \bar{\tau}_{zx}$ with $|\nabla\bar{p}| \equiv |\partial\bar{p}/\partial\bar{z}|$), and to

$$\frac{\partial\bar{\sigma}_n}{\partial\bar{z}} = \frac{\bar{\sigma}_n}{S\bar{v}_z}\frac{\partial\bar{q}_x}{\partial\bar{x}} - \frac{\bar{v}_x}{\bar{v}_z}\frac{\partial\bar{\sigma}_n}{\partial\bar{x}} + \frac{\bar{\sigma}_n}{\bar{\tau}}\left(\frac{\bar{v}_x}{\bar{v}_z}\frac{\partial\bar{\tau}}{\partial\bar{x}} + \frac{\partial\bar{\tau}}{\partial\bar{z}}\right) \tag{11}$$

and

$$\frac{\partial\bar{v}_x}{\partial\bar{x}} = -\frac{\partial\bar{q}_x}{\partial\bar{x}} - \frac{\partial\bar{v}_z}{\partial\bar{z}} \tag{12}$$

for the conservation of mass. The rheological description given in the main text gives

$$\frac{\partial\bar{v}_z}{\partial\bar{x}} = \bar{\sigma}_n J \tag{13}$$

In cylindrical coordinates (i.e., pipe flow), projecting Eq. 6 onto the axes and using the characteristic scales introduced in Eq. 4 results in

$$\begin{gathered}\frac{1}{\phi}\left(\bar{v}_r\frac{\partial\phi}{\partial\bar{r}} + \bar{v}_z\frac{\partial\phi}{\partial\bar{z}}\right) - \frac{1}{\bar{r}}\frac{\partial}{\partial\bar{r}}(\bar{r}\bar{q}_r) - \delta\frac{\partial\bar{q}_z}{\partial\bar{z}} = 0\\ \frac{1}{\bar{r}}\frac{\partial}{\partial\bar{r}}(\bar{r}\bar{v}_r) + \frac{\partial\bar{v}_z}{\partial\bar{z}} + \frac{1}{\bar{r}}\frac{\partial}{\partial\bar{r}}(\bar{r}\bar{q}_r) + \delta\frac{\partial\bar{q}_z}{\partial\bar{z}} = 0\\ \frac{1}{\bar{r}}\frac{\partial}{\partial\bar{r}}(\bar{r}\bar{\tau}_{rr}) + \delta\frac{\partial\bar{\tau}_{rz}}{\partial\bar{z}} - \frac{1}{\delta}\frac{\partial\bar{p}}{\partial\bar{r}} = 0\\ \frac{1}{\bar{r}}\frac{\partial}{\partial\bar{r}}(\bar{r}\bar{\tau}_{zr}) + \delta\frac{\partial\bar{\tau}_{zz}}{\partial\bar{z}} - \frac{\partial\bar{p}}{\partial\bar{z}} = 0\end{gathered} \tag{14}$$

and, similarly, the relative phase slip vector can be decomposed in

$$\begin{aligned}\bar{q}_r &= -\frac{\kappa}{\delta}\frac{\partial\bar{p}_f}{\partial\bar{r}} = -\kappa\left(\frac{1}{\delta}\frac{\partial\bar{p}}{\partial\bar{r}} - \frac{\partial\bar{p}_s}{\partial\bar{r}}\right)\\ \bar{q}_z &= -\kappa\frac{\partial\bar{p}_f}{\partial\bar{z}} = -\kappa\left(\frac{\partial\bar{p}}{\partial\bar{z}} - \delta\frac{\partial\bar{p}_s}{\partial\bar{z}}\right)\end{aligned} \tag{15}$$

Again assuming $\delta \ll 1$ (i.e., a is much smaller than the radius R of the conduit), Eq. 15 reduces to

$$\begin{aligned}\bar{q}_r &= -\kappa\left(\frac{1}{\bar{r}}\frac{\partial}{\partial\bar{r}}(\bar{r}\bar{\tau}_{rr}) - \frac{\partial\bar{p}_s}{\partial\bar{r}}\right) = -\frac{\kappa}{\bar{r}}\frac{\partial}{\partial\bar{r}}(\bar{r}\bar{\sigma}_n)\\ \bar{q}_z &= -\kappa\frac{\partial\bar{p}}{\partial\bar{z}}\end{aligned} \tag{16}$$

Similarly, Eq. 14 reduces to

$$\frac{1}{\bar{r}}\frac{\partial}{\partial\bar{r}}(\bar{r}\bar{\tau}_{zr}) = \frac{\partial\bar{p}}{\partial\bar{z}} \tag{17}$$

for the conservation of momentum, imply that $\bar{\tau} = \frac{1}{2}|\nabla\bar{p}|\bar{r}$ (defined as $\bar{\tau} \equiv \bar{\tau}_{zr}$ with $|\nabla\bar{p}| \equiv |\partial\bar{p}/\partial\bar{z}|$), and to

$$\frac{\partial\bar{\sigma}_n}{\partial\bar{z}} = \frac{1}{\bar{r}}\frac{\bar{\sigma}_n}{S\bar{v}_z}\frac{\partial}{\partial\bar{r}}(\bar{r}\bar{q}_r) - \frac{\bar{v}_r}{\bar{v}_z}\frac{\partial\bar{\sigma}_n}{\partial\bar{r}} + \frac{\bar{\sigma}_n}{\bar{\tau}}\left(\frac{\bar{v}_r}{\bar{v}_z}\frac{\partial\bar{\tau}}{\partial\bar{r}} + \frac{\partial\bar{\tau}}{\partial\bar{z}}\right) \tag{18}$$

and

$$\frac{1}{\bar{r}}\frac{\partial}{\partial\bar{r}}(\bar{r}\bar{v}_r) = -\frac{1}{\bar{r}}\frac{\partial}{\partial\bar{r}}(\bar{r}\bar{q}_r) - \frac{\partial\bar{v}_z}{\partial\bar{z}} \tag{19}$$

for the conservation of mass. Eq. 13 then becomes

$$\frac{\partial\bar{v}_z}{\partial\bar{r}} = \bar{\sigma}_n J \tag{20}$$

Solving Eqs. 9–13 or 16–20 require initial and boundary conditions. At the inlet $z = 0$, we assume a uniform distribution of crystals $\phi = \phi_0$ across the system, as well as a uniform axial velocity, resulting in a parabolic flow, following Poiseuille's law, such that $\bar{v}_z = 3(1-\bar{x}^2)/2$ in Cartesian coordinates and $\bar{v}_z = 2(1-\bar{r}^2)$ in cylindrical coordinates. A no-slip condition is imposed at the walls of the conduit (i.e., $\bar{v}_x = \bar{v}_r = \bar{v}_z = 0$). The numerical procedure follows three steps to advance the solution from $\bar{z}$ to $\bar{z} + \Delta\bar{z}$, which are repeated until an arrest criterion is met (e.g., $\bar{z} = 1$). In the first step, Eq. 11 or 18 is solved for $\bar{\sigma}_n$ using a backward time, centred space finite-difference scheme coupled with a relaxed fixed-point iteration method assuming a boundary of symmetry at $\bar{x} = \bar{r} = 0$ and $\bar{q}_x = \bar{q}_r = 0$ at $\bar{x} = \bar{r} = 1$. As a second step, the mixture pressure gradient $|\nabla\bar{p}|$ is found using a sub-iterative procedure $|\nabla\bar{p}|^{(i+1)} = |\nabla\bar{p}|^{(i)}/\langle\bar{v}_z\rangle^{(i)}$ via the global continuity condition $\langle\bar{v}_z\rangle = 1$ with the gap-averaged vertical velocity given by $\langle\bar{v}_z\rangle = -\int_0^1 J\bar{\sigma}_n\bar{x}\mathrm{d}\bar{x}$ and $\langle\bar{v}_z\rangle = -\int_0^1 J\bar{\sigma}_n\bar{r}^2\mathrm{d}\bar{r}$ in Cartesian and cylindrical coordinates, respectively, since J is a function of $|\nabla\bar{p}|$ via μ. As a third step, ϕ is retrieved using Eq. 2, and finally, $\bar{v}_x$ or $\bar{v}_r$ and $\bar{v}_z$ by integrating Eq. 12 or 19 and Eq. 13 or 20, respectively.

Flow development length

To compute L_d via Eq. 5, we have to first use Eq. 2 to compute μ. Next, we require $\mathrm{d}\mu/\mathrm{d}\phi$ to compute $S(\phi)$, and so we differentiate Eq. 2 to find an analytical form as

$$\frac{\mathrm{d}\mu}{\mathrm{d}\phi} = -\frac{1}{\beta} - J\left(\frac{2}{\phi} + \frac{5}{2}\right) - \frac{2}{\phi_j}\left[J + \left(\frac{5}{2}\phi_j + 2\right)J^{\frac{1}{2}}\right]\left(1 - \frac{\phi}{\phi_j}\right) \tag{21}$$

Then this allows us to compute $S(\phi) = -(\mu/\phi)\mathrm{d}\phi/\mathrm{d}\mu$ for a given ϕ_0. In turn, we can then use Eq. 5 as given in the main text to compute the flow development length for any given inlet crystal volume fraction ϕ_0 (see Fig. 3 for example calculations across all ϕ_0).

Justification of volcanological parameters

The inputs to the dimensional form of the conduit model (Fig. 3a–d) are the inlet crystallinity ϕ_0, the crystal size a, the conduit radius R, and the conduit length L_f. For Kilauea, we take $\phi_0 = 0.1$ (ref. 55), $a = 600$ μm (referring to olivine phenocrysts; ref. 50), $R = 20$m (ref. 55), and $L_f = 2$ km (ref. 55). For Mt Unzen we take $\phi_0 = 0.55$ (ref. 7), $a = 300$ μm (ref. 56), $R = 25$m (ref. 57), and $L_f = 7.5$ km (ref. 58). Then, for the general scaling given in Fig. 3e, we do two things: (1) we compute the development length for some generic volcanological parameters (the grey shaded area), and (2) we show the conduit length L_f and crystallinity ranges for some key volcanoes. For the former, the grey shaded area is L_d bounded by $2.5 \leq R \leq 50$ m and $10^{-5} \leq a \leq 10^{-3}$m. For the latter, we use inputs ϕ_0 and L_f only. When L_f is not directly available, we rely instead on petrologic estimations of storage pressures. For Etna, we take $0.05 \leq \phi_0 \leq 0.15$ (ref. 55), and $L_f = 9$ km (ref. 55). For Volcán de Colima, we take $0.5 \leq \phi_0 \leq 0.7$ (ref. 59), and $3 \leq L_f \leq 7$ km (ref. 58). For Mt Pelée we take $0.4 \leq \phi_0 \leq 0.55$ (ref. 60), and $L_f = 17.5$ km (ref. 58). For Mt St Helens, we take $0.4 \leq \phi_0 \leq 0.72$ (ref. 61), and $8.5 \leq L_f \leq 11.5$ km (refs. 62,63). For Santiaguito, we take $0.35 \leq \phi_0 \leq 0.47$ (ref. 64), and $6 \leq L_f \leq 7.5$ km (ref. 64).

Effects of spreading arising from gravity

For simplicity, we omit the effect of gravity in our simulations (cf. Eq. 6). To justify this, we compute two competing driving pressure gradients in our systems. First, the pressure gradient driving crystal migration is $\nabla p_m \propto -d\sigma_n/dx$. Second, the pressure gradient that would be acting to spread the crystals under gravity is $\nabla p_g \propto \Delta\rho g(L_f - z)d\phi/dx$, where $\Delta\rho = \rho_s - \rho_f$ is the density contrast between the crystals and the melt phase. The subscripts 'm' and 'g' refer to 'migration' and 'gravity', respectively. If we use a crystal density of 2600 kg.m^{-3} and a melt density of 2000 kg.m^{-3}, we can look for which of these pressure gradients is larger in our simulations. If $\nabla p_m < \nabla p_g$, then gravitational spreading of the central plug of crystals will outcompete the pressures acting to keep the plug intact, and migration will be reversed or not occur at all. We performed checks on all of our dimensional simulation outputs to check if $\nabla p_m > \nabla p_g$. There are conditions for which $\nabla p_m < \nabla p_g$ but these appear to be the preserve of systems that have very narrow conduit dimensions down to a conduit width of around 1 m, and/or relatively low melt viscosity (i.e., $\lesssim 10^7$ Pa.s). These effects do not influence our primary finding that in nature migration is rarely acting and that instead, the contribution of crystals to conduit flow is Newtonian.

Code availability

The conduit flow model Cython code is provided a supplementary file package, including a guidance documentation.

Received: 11 December 2023; Accepted: 1 July 2024;
Published online: 20 July 2024

References

1. Cassidy, M., Manga, M., Cashman, K. & Bachmann, O. Controls on explosive-effusive volcanic eruption styles. *Nat. Commun.* **9**, 2839 (2018).
2. Mader, H. M., Llewellin, E. W. & Mueller, S. P. The rheology of two-phase magmas: a review and analysis. *J. Volcanol. Geotherm. Res.* **257**, 135–158 (2013).
3. Llewellin, E. W., Mader, H. M. & Wilson, S. D. R. The constitutive equation and flow dynamics of bubbly magmas. *Geophys. Res. Lett.* **29**, 23–24 (2002).
4. Manga, M., Castro, J., Cashman, K. V. & Loewenberg, M. Rheology of bubble-bearing magmas. *J. Volcanol. Geotherm. Res.* **87**, 15–28 (1998).
5. Caricchi, L. et al. Non-Newtonian rheology of crystal-bearing magmas and implications for magma ascent dynamics. *Earth Planet Sci. Lett.* **264**, 402–419 (2007).
6. Costa, A., Caricchi, L. & Bagdassarov, N. A model for the rheology of particle-bearing suspensions and partially molten rocks. *Geochem. Geophys. Geosyst.* **10**, Q03010 (2009).
7. Lavallée, Y., Hess, K.-U., Cordonnier, B. & Dingwell, D. B. Non-Newtonian rheological law for highly crystalline dome lavas. *Geology* **35**, 843–846 (2007).
8. Mueller, S., Llewellin, E. W. & Mader, H. M. The effect of particle shape on suspension viscosity and implications for magmatic flows. *Geophys. Res. Lett.* **38**, L13316 (2011).
9. Gaunt, H., Sammonds, P., Meredith, P., Smith, R. & Pallister, J. Pathways for degassing during the lava dome eruption of Mount St. Helens 2004–2008. *Geology* **42**, 947–950 (2014).
10. Kendrick, J. E. et al. Extreme frictional processes in the volcanic conduit of Mount St. Helens (USA) during the 2004-2008 eruption. *J. Struct. Geol.* **38**, 61–76 (2012).
11. Lavallée, Y. et al. Transient conduit permeability controlled by a shift between compactant shear and dilatant rupture at Unzen volcano (Japan). *Solid Earth* **13**, 875–900 (2022).
12. Kendrick, J. et al. Volcanic drumbeat seismicity caused by stick-slip motion and magmatic frictional melting. *Nat. Geosci.* **7**, 438–442 (2014).
13. Lensky, N., Sparks, R., Navon, O. & Lyakhovsky, V. Cyclic activity at Soufrière Hills Volcano, Montserrat: degassing-induced pressurization and stick-slip extrusion. *Geol. Soc. Lond. Spec. Publ.* **307**, 169–188 (2008).
14. Arzilli, F. et al. Magma fragmentation in highly explosive basaltic eruptions induced by rapid crystallization. *Nat. Geosci.* **12**, 1023–1028 (2019).
15. Degruyter, W., Bachmann, O., Burgisser, A. & Manga, M. The effects of outgassing on the transition between effusive and explosive silicic eruptions. *Earth Planet. Sci. Lett.* **349–350**, 161–170 (2012).
16. Gonnermann, H. M. & Manga, M. Explosive volcanism may not be an inevitable consequence of magma fragmentation. *Nature* **426**, 432–435 (2003).
17. Boyer, F., Guazzelli, É. & Pouliquen, O. Unifying suspension and granular rheology. *Phys. Rev. Lett.* **107**, 188301 (2011).
18. Mueller, S., Llewellin, E. W. & Mader, H. M. The rheology of suspensions of solid particles. *Proc. R. Soc. A* **466**, 1201–1228 (2010).
19. Champallier, R., Bystricky, M. & Arbaret, L. Experimental investigation of magma rheology at 300 MPa: from pure hydrous melt to 76 vol.% of crystals. *Earth Planet. Sci. Lett.* **267**, 571–583 (2008).
20. Cordonnier, B. et al. The viscous-brittle transition of crystal-bearing silicic melt: direct observation of magma rupture and healing. *Geology* **40**, 611–614 (2012).
21. Lejeune, A.-M. & Richet, P. Rheology of crystal-bearing silicate melts: an experimental study at high viscosities. *J. Geophys. Res.* **100**, 4215–4229 (1995).
22. Picard, D., Arbaret, L., Pichavant, M., Champallier, R. & Launeau, P. The rheological transition in plagioclase-bearing magmas. *J. Geophys. Res.* **118**, 1363–1377 (2013).
23. Pistone, M. et al. Deformation experiments of bubble- and crystal-bearing magmas: Rheological and microstructural analysis. *J. Geophys. Res.* **117**, B05208 (2012).
24. Stickel, J. J. & Powell, R. L. Fluid mechanics and rheology of dense suspensions. *Annu. Rev. Fluid Mech.* **37**, 129–149 (2005).
25. Vasseur, J., Wadsworth, F. B. & Dingwell, D. B. Shear thinning and brittle failure in crystal-bearing magmas arise from local non-Newtonian effects in the melt. *Earth Planet. Sci. Lett.* **603**, 117988 (2023).
26. Webb, S. L. & Dingwell, D. B. Non-Newtonian rheology of igneous melts at high stresses and strain rates: experimental results for

rhyolite, andesite, basalt, and nephelinite. *J. Geophys. Res.* **95**, 15695–15701 (1990).
27. Cordonnier, B., Schmalholz, S. M., Hess, K.-U. & Dingwell, D. B. Viscous heating in silicate melts: an experimental and numerical comparison. *J. Geophys. Res.* **117**, B02203 (2012).
28. Kendrick, J. E. et al. Tracking the permeable porous network during strain-dependent magmatic flow. *J. Volcanol. Geotherm. Res.* **260**, 117–126 (2013).
29. Lavallée, Y. et al. Seismogenic lavas and explosive eruption forecasting. *Nature* **453**, 507–510 (2008).
30. Lavallée, Y. & Kendrick, J. Strain localization in magmas. *Rev. Miner. Geochem.* **87**, 721–765 (2022).
31. Lecampion, B. & Garagash, D. I. Confined flow of suspensions modelled by a frictional rheology. *J. Fluid Mech.* **759**, 197–235 (2014).
32. Oh, S., Song, Y. Q., Garagash, D. I., Lecampion, B. & Desroches, J. Pressure-driven suspension flow near jamming. *Phys. Rev. Lett.* **114**, 088301 (2015).
33. Dbouk, T., Lobry, L. & Lemaire, E. Normal stresses in concentrated non-Brownian suspensions. *J. Fluid Mech.* **715**, 239–272 (2013).
34. Tapia, F., Shaikh, S., Butler, J. E., Pouliquen, O. & Guazzelli, E. Rheology of concentrated suspensions of non-colloidal rigid fibres. *J. Fluid Mech.* **827**, R5 (2017).
35. Maron, S. & Pierce, P. Application of Ree-Eyring generalized flow theory to suspensions of spherical particles. *J. Colloid Sci.* **11**, 80–95 (1956).
36. Hampton, R. E., Mammoli, A. A., Graham, A. L., Tetlow, N. & Altobelli, S. A. Migration of particles undergoing pressure-driven flow in a circular conduit. *J. Rheol.* **41**, 621–640 (1997).
37. Torquato, S. *Random Heterogeneous Materials: Microstructure and Macroscopic Properties*. vol. 16 (Springer Science & Business Media, New York, NY, 2002).
38. Lyon, M. & Leal, L. An experimental study of the motion of concentrated suspensions in two-dimensional channel flow. Part 2. Bidisperse systems. *J. Fluid Mech.* **363**, 57–77 (1998).
39. Lyon, M. & Leal, L. An experimental study of the motion of concentrated suspensions in two-dimensional channel flow. Part 1. Monodisperse systems. *J. Fluid Mech.* **363**, 25–56 (1998).
40. Davis, R. H. & Acrivos, A. Sedimentation of noncolloidal particles at low Reynolds numbers. *Annu. Rev. Fluid Mech.* **17**, 91–118 (1985).
41. Goto, A. et al. Rigid migration of Unzen lava rather than flow. *J. Volcanol. Geotherm. Res.* **407**, 107073 (2020).
42. Seropian, G., Rust, A. C. & Sparks, R. S. J. The gravitational stability of lenses in magma mushes: confined Rayleigh-Taylor instabilities. *J. Geophys. Res.* **123**, 3593–3607 (2018).
43. Wallace, P. A. et al. Petrological architecture of a magmatic shear zone: a multidisciplinary investigation of strain localisation during magma ascent at Unzen Volcano, Japan. *J. Petrol.* **60**, 791–826 (2019).
44. Yilmaz, T. I. et al. Rapid alteration of fractured volcanic conduits beneath Mt Unzen. *Bull. Volcanol.* **83**, 34 (2021).
45. Wadsworth, F. B. et al. Combined effusive-explosive silicic volcanism straddles the multiphase viscous-to-brittle transition. *Nat. Commun.* **9**, 1–8 (2018).
46. Dingwell, D. B. & Webb, S. L. Structural relaxation in silicate melts and non-Newtonian melt rheology in geologic processes. *Phys. Chem. Min.* **16**, 508–516 (1989).
47. Castro, J. M. & Dingwell, D. B. Rapid ascent of rhyolitic magma at Chaitén Volcano, Chile. *Nature* **461**, 780–783 (2009).
48. Tian, Y. & Shan, Y. The diversity of flow structures in felsic dykes. *J. Geol. Soc. Lond.* **168**, 1001–1011 (2011).
49. Russell, J. & Jones, T. Transport and eruption of mantle xenoliths creates a lagging problem. *Commun. Earth Environ.* **4**, 177 (2023).
50. Schwindinger, K. R. & Anderson, A. T. Synneusis of Kilauea Iki olivines. *Contrib. Mineral. Petrol.* **103**, 187–198 (1989).
51. Di Vaira, N. J., Łaniewski-Wołłk, Ł., Johnson, R. L., Aminossadati, S. M. & Leonardi, C. R. Influence of particle polydispersity on bulk migration and size segregation in channel flows. *J. Fluid Mech.* **939**, A30 (2022).
52. Llewellin, E. W. & Manga, M. Bubble suspension rheology and implications for conduit flow. *J. Volcanol. Geotherm. Res.* **143**, 205–217 (2005).
53. Kendrick, J. E. et al. Crystal plasticity as an indicator of the viscous-brittle transition in magmas. *Nat. Commun.* **8**, 1926 (2017).
54. Costa, A., Melnik, O. & Vedeneeva, E. Thermal effects during magma ascent in conduits. *J. Geophys. Res.* **112**, B12205 (2007).
55. La Spina, G. et al. Explosivity of basaltic lava fountains is controlled by magma rheology, ascent rate and outgassing. *Earth Planet. Sci. Lett.* **553**, 116658 (2021).
56. Noguchi, S., Toramaru, A. & Nakada, S. Relation between microlite textures and discharge rate during the 1991–1995 eruptions at Unzen, Japan. *J. Volcanol. Geotherm. Res.* **175**, 141–155 (2008).
57. Goto, A. A new model for volcanic earthquake at Unzen Volcano: melt rupture model. *Geophys. Res. Lett.* **26**, 2541–2544 (1999).
58. Cassidy, M. et al. Explosive eruptions with little warning: experimental petrology and volcano monitoring observations from the 2014 eruption of Kelud, Indonesia. *Geochem. Geophys. Geosyst.* **20**, 4218–4247 (2019).
59. Luhr, J. F. Petrology and geochemistry of the 1991 and 1998-1999 lava flows from Volcán de Colima, México: Implications for the end of the current eruptive cycle. *J. Volcanol. Geotherm. Res.* **117**, 169–194 (2002).
60. Martel, C. & Poussineau, S. Diversity of eruptive styles inferred from the microlites of Mt Pelée andesite (Martinique, Lesser Antilles). *J. Volcanol. Geotherm. Res.* **166**, 233–254 (2007).
61. Rutherford, M. J., Sigurdsson, H., Carey, S. & Davis, A. The May 18, 1980, eruption of Mount St. Helens. 1. Melt composition and experimental phase equilibria. *J. Geophys. Res.* **90**, 2929–2947 (1985).
62. Carey, S. & Sigurdsson, H. The May 18, 1980 eruption of Mount St. Helens: 2. Modeling of dynamics of the Plinian phase. *J. Geophys. Res.* **90**, 2948–2958 (1985).
63. Scandone, R. & Malone, S. Magma supply, magma discharge and readjustment of the feeding system of Mount St. Helens during 1980. *J. Volcanol. Geotherm. Res.* **23**, 239–262 (1985).
64. Holland, A., Watson, I., Phillips, J., Caricchi, L. & Dalton, M. Degassing processes during lava dome growth: Insights from Santiaguito lava dome, Guatemala. *J. Volcanol. Geotherm. Res.* **202**, 153–166 (2011).
65. Rodriguez, B. E., Kaler, E. W. & Wolfe, M. S. Binary mixtures of monodisperse latex dispersions. 2. Viscosity. *Langmuir* **8**, 2382–2389 (1992).
66. Segrè, P. N., Meeker, S. P., Pusey, P. N. & Poon, W. C. K. Viscosity and structural relaxation in suspensions of hard-sphere colloids. *Phys. Rev. Lett.* **75**, 958–961 (1995).
67. Bonnoit, C., Darnige, T., Clement, E. & Lindner, A. Inclined plane rheometry of a dense granular suspension. *J. Rheol.* **54**, 65–79 (2010).
68. Ovarlez, G., Bertrand, F. & Rodts, S. Local determination of the constitutive law of a dense suspension of noncolloidal particles through magnetic resonance imaging. *J. Rheol.* **50**, 259–292 (2006).
69. Zarraga, I., Hill, D. & Leighton, D. Jr The characterization of the total stress of concentrated suspensions of noncolloidal spheres in Newtonian fluids. *J. Rheol.* **44**, 185–220 (2000).

Acknowledgements

We thank the editor Domenico Doronzo, as well as Chiara Montagna and one anonymous reviewer for their thorough reviews of our work, which improved its quality and impact. We are grateful for discussions with Laurence Wayne, Luiz Pereira, Edward Llewellin, Alexandra Kushnir, Brice Lecampion, Dmitry Garagash, Ceri Allgood, Michael Manga, Kelly Russell, David Hyman, Melissa Drignon, and Nick Petford. We acknowledge funding provided by the ERC (European Research Council) via Advanced Grant EAVESDROP

(834225) to D.B.D. and Consolidator Grant MODERATE (10100165) to Y.L. This research project/publication was supported by LMUexcellent, funded by the Federal Ministry of Education and Research (BMBF) and the Free State of Bavaria under the Excellence Strategy of the Federal Government and the Länder.

Author contributions
J.V. and F.B.W. conceptualized the study and analysed the data. F.B.W. and J.V. led the data compilation for volcanic scenarios and manuscript drafting. D.B.D. and Y.L. provided volcanological insights and context for the model application. All authors contributed to the manuscript writing and editing.

Funding
Open Access funding enabled and organized by Projekt DEAL.

Competing interests
The authors declare no competing interests.

Additional information
Supplementary information The online version contains supplementary material available at https://doi.org/10.1038/s43247-024-01556-8.

Correspondence and requests for materials should be addressed to Jérémie Vasseur.

Peer review information *Communications Earth & Environment* thanks Oleg Melnik and Chiara Montagna for their contribution to the peer review of this work. Primary Handling Editors: Domenico Doronzo and Carolina Ortiz Guerrero. A peer review file is available.